Mechanical Systems and Signal Processing 187 (2023) 109952

Contents lists available at ScienceDirect

Mechanical Systems and Signal Processing

journal homepage: www.elsevier.com/locate/ymssp

Influence of mesoscale friction interface geometry on the nonlinear dynamic response of large assembled structures

Jie Yuan [a,*], Loic Salles [b,c], David Nowell [c,d], Christoph Schwingshackl [c]

[a] Aerospace Centre of Excellence, Department of Mechanical and Aerospace Engineering, University of Strathclyde, Glasgow, G1 1XQ, UK
[b] Mechanical Aspects of Turbomachinery and Aerospace Propulsion, University of Liège, 4000 Liège, Belgium
[c] Vibration University Technology Centre, Department of Mechancial Engineering, Imperial College London, SW7 2AZ, London, UK
[d] Department of Engineering Science, University of Oxford, Parks Road, Oxford, OX1 3PJ, UK

ARTICLE INFO

Communicated by M. Krack

Keywords:
Multi-scale analysis
Friction interface
Assembled structures
Damped nonlinear modal analysis
Contact mechanics

ABSTRACT

Friction interfaces are unavoidable components of large engineering assemblies since they enable complex designs, ensure alignment, and enable the transfer of mechanical loads between the components. Unfortunately, they are also a major source of nonlinearities and uncertainty in the static and dynamic response of the assembly, due to the complex frictional physics occurring at the interface. One major contributor to the nonlinear dynamic behavior of the interface is the mesoscale geometry of a friction interface. Currently, the effects of the interface geometry on the nonlinear dynamic response is often ignored in the analysis due to the high computational cost of discretizing the interface to such fine levels for classical finite element analysis. In this paper, the influence of mesoscale frictional interface geometries on the nonlinear dynamic response is investigated through an efficient multi-scale modeling framework based on the boundary element method. A highly integrated refined contact analysis, static analysis, and nonlinear modal analysis approach are presented to solve a multi-scale problem where mesoscale frictional interfaces are embedded into the macroscale finite element model. The efficiency of the framework is demonstrated and validated against an existing dovetail dogbone test rig. Finally, the effects of different mesoscale interface geometries such as surface waviness and edge radius, are numerically investigated, further highlighting the influence of mesoscale interface geometries on the nonlinear dynamics of jointed structures and opening a new research direction for the design of friction interfaces in friction involved mechanical systems.

1. Introduction

Frictional interfaces can be found in almost all large engineering systems that consist of multiple components. These interfaces are widely regarded [1–4] as the main source of uncertainty and nonlinearity in assembled structures since they can significantly reduce overall stiffness, shift resonance frequencies and increase structural damping. The latter makes them of particular interest for the design of dry friction dampers, which can significantly reduce vibration levels, such as Under-Platform Dampers (UPDs) for turbine blades [5] and ring dampers for integrally bladed disks (blisks) [6,7]. To ensure a reliable design for mechanical structures with frictional interfaces, their nonlinear effects on the dynamic response must be accurately predicted [8,9].

Previous studies [10,11] have shown how frictional interfaces can significantly affect the nonlinear dynamic response of large aero-engine structures. Petrov [10,11] carried out a numerical study on the performance of UPD designs for different contact

* Corresponding author.
E-mail address: jie.yuan@strath.ac.uk (J. Yuan).

https://doi.org/10.1016/j.ymssp.2022.109952
Received 18 June 2022; Received in revised form 10 November 2022; Accepted 11 November 2022
Available online 1 December 2022

parameters at the blade-damper interface, such as friction coefficient, contact stiffness, clearance, and interference. A similar study was also performed by Krack et al. [12] to analyze the uncertainties associated with contact parameters showing the significant influences of these uncertainties on the nonlinear dynamical response. The effects of macro-scale frictional interface designs have been also widely studied. The macro-scale interface refer to different geometries such as length, width and global shape of the interface at a scale of centimeter that can be easily used as manufacturing parameters [13]. Sun et al. [4] proposed a parametric model of UPDs to investigate the effects of contact angle, length, and position of the platform of a UDP on nonlinear modal properties of turbine blades. Tang and Epureanu [14] investigated four global geometric parameters of a V-shaped friction ring damper, including the length of the friction interface and the angle between the two surfaces, on the dynamic response of a blisk. Panning et al. [15] evaluated the effects of the contact geometry on damping effectiveness by varying the geometry of both the blade platform and the friction damper. Hüls et al. [16] studied the effects of geometrical parameters of turbine friction dampers on the nonlinear dynamic response. Yuan et al. [17] further optimized the geometrical parameters of a wedged UPD (such as the height and width) using a robust approach considering the manufacturing uncertainties. All of these studies have shown the importance of contact parameters (such as contact stiffness, and friction coefficients) and the macro-scale geometries of the frictional interface but a lot of uncertainties remains due to smaller scale variations at the micro/mesoscale. The mesoscale of a friction interface refers to the surface curvature while the micro-scale refers to the surface roughness [13].

Because of the high computational expense of using a Finite Element (FE) approach to discretize micro/mesoscale features, there are very few numerical studies so far to address this multi-scale challenge. To reduce some of the computational cost of a full 3D FE modeling approach, alternatively, the elastic contact problem can be analytically formulated to estimate the behavior of a frictional interface, particularly for completely smooth surfaces. For a surface with micro-scale asperities, a compliant model was developed [18] which considers a statistical distribution of asperities. Such a statistical approach considers the effects of the surface asperities in a statistically averaged sense, which is more computationally feasible. For the normal contact problem, either a linear penalty stiffness approach [19] or a nonlinear penalty model [20] can be used to represent the asperity effects. Alternatively, fractal and self-affine geometries can be used to model the roughness at all length scales [21]. To couple the effects of micro-scale roughness with the dynamic response of the system, zero-thickness elements have been modified to include multi-scale contact constitutive laws [22]. A semi-analytical solver was also developed to include the effects of the surface roughness on the nonlinear dynamic response [23]. Although surface roughness at the micro-scale can influence the contact stiffness, it is not very significant in the nonlinear dynamic response [13,23].

Experimentally, it was recently established that mesoscale variations at the interface (eg. waviness due to manufacturing tolerances) appear to lead to a much larger variation in the nonlinear dynamic response. Allara et al. [24] studied the effects of a ‘crowned’ frictional interface (at the mesoscale level) on dovetail blade root behavior. In comparison to a flat-to-flat interface, the crowned interface showed much smoother damping behavior with increasing excitation levels. A similar impact of a non-conforming interface was observed in an UPD test rig [25], where only the accurate and detailed discretization of the interface geometry enabled a model validation. Gastaldi et al. [26] experimentally studied the influence of different surface finishes at micro and mesoscale on the performance of UPDs, indicating the significance of contact conditions on the dynamic properties. Recently, Sun et al. [7] investigated the influence of different levels of waviness of the friction interface geometry on the dynamic response of a blisk with a ring damper. It has been shown that the waviness introduced into the interface can significantly change the initial normal pressure and gap distribution and hence impact the dynamic response significantly. Based on these experimental findings, the mesoscale contact geometry appears to be a determining factor when predicting the nonlinear dynamic response but modeling such detailed interface geometries, using a direct FE approach, can become extremely computationally expensive and up to now, the multi-scale approach seems to only include micro, but not these mesoscale features.

Advanced multi-scale approaches have been recently actively explored to reduce the computational cost of detailed interface modeling. A multi-scale approach was originally proposed by Gallego [27] to evaluate the influence of fretting wear on a bladed disk system. Such an approach allows a fine discretization of the contact zone and fast computation of fretting wear on the contact interfaces without the need for detailed FE models. The method was then extended by Salles et al. [28,29] to couple the fast dynamic analysis with the slow tribological analysis based on a dynamic Lagrangian frequency-time scheme. This approach was further expanded by Armand et al. [23,30] to simulate the effects of the micro-scale surface roughness and fretting wear on the nonlinear dynamic response. An alternative multi-scale framework was recently proposed by Balaji et al. [22] for modeling the dynamics of bolted structures through zero-thickness elements and quasi-static modal analysis. However, the effects of mesoscale frictional interface geometry have not been thoroughly investigated.

In addition to the investigation of the influence of mesoscale friction interfaces, this work will also improve the efficiency of the multi-scale approach originally presented in [23]. As an alternative to forced response frequency analysis, the concept of nonlinear modal analysis was originally proposed by Rosenberg [31] and extended into non-conservative systems by Shaw and Pierre [32]. It can be used to obtain resonance frequency and damping levels over a wide range of excitation from a single simulation that greatly increases the computational efficiency. There are two main approaches, one is based on the Extended Periodic Motion Concept (EPMC) [33] and the other is based on Complex Nonlinear Modal (CNM) analysis [34]. Both of these approaches can be used to obtain the nonlinear modal properties over a wide range of energy levels. CNM is based on the damped motion concept while EPMC is based on the periodic motion by adding an artificial damping term [35,36]. Based on nonlinear normal modes, the corresponding resonant forced response can be effectively evaluated using single mode theory [37] or extended energy balance approaches [38]. The applicability of these two approaches to an industrial case study of an aero engine fan blade has been shown in [39]. Recently, quasi-static modal analysis was further introduced to obtain resonant frequencies and damping [40–42] of nonlinear mechanical systems by applying a distributed load to the structure that would deflect the linear structure into a user-specified mode shape.

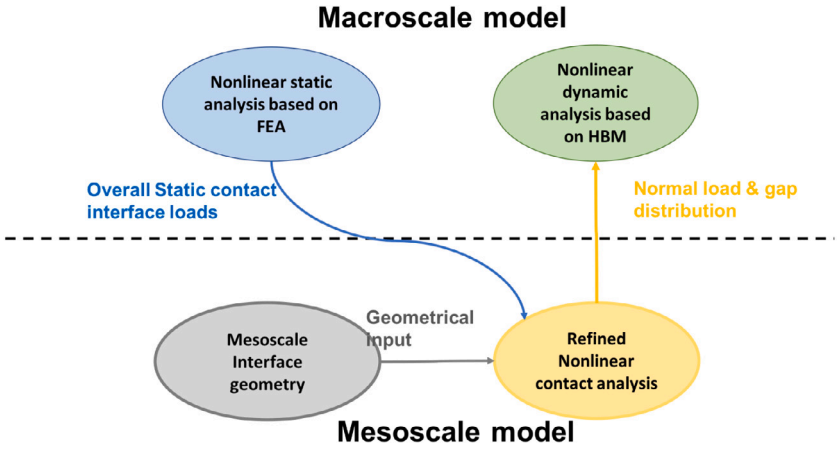

Fig. 1. A general structure of the multi-scale approach.

Comparing to EPMC and CNM [42], this quasi-static approach can achieve higher computational efficiency but the accuracy cannot be fully guaranteed in the presence of modal interaction and high excitation levels.

Overall, the main aim of this study is to investigate the influence of mesoscale contact geometry on the nonlinear dynamics of large assembled structures through a multi-scale approach. The principle of this approach consists of embedding the mesoscale frictional interfaces, obtained by an existing semi-analytical solver [23], into the coarser FE model used for the nonlinear dynamical analysis. The dynamic analysis solver will further integrate advanced nonlinear modal analysis and adaptive reduced order modeling techniques [43,44] into the multi-scale modeling framework [23] to increase the computational efficiency. The proposed framework will be used to, for the first time, assess the influence of a mesoscale interface geometry on the dynamic response of assembled structures. The impact of mesoscale interface geometries (such as radius, and interface topology) and contact parameters (including friction coefficients and pre-loading) will be shown for an existing blade root dog bone test rig [45,46].

2. Methodology of multi-scale analysis

Fig. 1 presents the methodology of the multi-scale modeling approach. Nonlinear dynamic and static analysis of the entire system is performed using a macro-scale FE model while nonlinear contact analysis for the local frictional interfaces is performed using mesoscale interface models. In this study, the micro-scale interface is defined as the friction interface representing surface roughness while the mesoscale refers to features such as surface waviness and curvature, which are often caused by machining tolerances. The macroscale interface refers to different geometries such as length, width, and global shape of the interface at a scale of centimeters [13]. The overall contact loads on the interfaces are initially evaluated via a nonlinear static analysis with a flat-on-flat contact interface. More refined contact analysis is then carried out with a semi-analytical solver based on the previously obtained overall contact loads. The calculated initial normal pressure and gap distributions are then used as the input parameters for the nonlinear dynamic analysis based on nonlinear modal analysis using the macro-scale FE model. The main advantage of this approach is that there is no need to re-mesh the contact surface for different mesoscale interface profiles since their features can be expressed in terms of load distribution and gap sizes in the macroscale model.

The original equation of motion, including static and dynamic loads, can be decomposed into a static problem (including only static loads) and a dynamic problem around the static equilibrium position (including only dynamic loads). The static contact loads obtained from the initial quasi-static analysis will provide the initial contact conditions for the subsequent nonlinear dynamical problem. A dynamic analysis around this static equilibrium position will then be used to obtain the nonlinear dynamical response. It should be noted that during a vibration cycle, the contact load can change due to the relative vibrational displacement of each contact pair, leading to a change in the overall stiffness and damping of the structure. More details about each part of the analysis are introduced in the following sections.

2.1. Nonlinear static analysis

The purpose of the nonlinear static analysis is to obtain the overall contact loads at the contact interface. It is performed to identify the nonlinear static equilibrium status using the macro-scale FE model. This nonlinear contact analysis can be carried out using any commercial software (ABAQUS in this study), where the surface-to-surface hard contact is defined at the interface. Eq. (1) shows the equation of this analysis where K is the linear joint stiffness; F_{nl} represents the nonlinear contact friction force as a function of relative displacement of the interface DOFs; $F_s(t)$ is the static loading vector applied to the system. Once equilibrium has been reached in the analysis, the obtained distribution of the normal contact loads from the interface can be summarized for a refined contact analysis including different mesoscale interface profiles.

$$\mathbf{K}\,u(t) + \mathrm{F}_{nl}(u(t)) = \mathrm{F}_s(t) \tag{1}$$

2.2. Refined contact analysis

The refined contact analysis will be conducted with an existing semi-analytical boundary element solver [47,48]. This solver is based on the projected conjugate gradient method [49] and a discrete-convolution Fast Fourier Transform (FFT). Based on the half-space assumption, the Boussinesq and Cerruti potentials are used to compute the elastic deflections of the surface in the normal and tangential directions due to the applied pressures and shear tractions which are obtained by the initial quasi-static analysis [50,51]. The main advantage of this semi-analytic solver is that a very fine contact mesh can be used to represent both micro/mesoscale friction interface features, such as surface roughness and waviness. The normal displacement u_z caused by a pressure distribution p is described by Eq. (2):

$$u_z(x,y) = \frac{1-\nu^2}{\pi E}\int_{-\infty}^{+\infty}\int_{-\infty}^{+\infty}\frac{p(\xi,\eta)}{\sqrt{(\xi-x)^2+(\eta-y)^2}}d\xi d\eta \tag{2}$$

where E and υ are the Young's modulus and Poisson ratio of the material respectively. Eq. (3) is the discretized form of Eq. (2) for a regular grid of $N_x \times N_y$ points, providing data for individual nodes in the mesh:

$$u_z(i,j) = K_{zz} \otimes p = \sum_{k=1}^{N_x}\sum_{l=1}^{N_y} p(k,l)K_{zz}(i-k,j-l) \tag{3}$$

where $K_{zz}(i,j)$ are the discrete influence coefficients that give the normal displacement resulting from unit pressure on the element centered on the grid point (i,j); $\otimes$ denotes the discrete convolution product. During the solution process, the normal contact problem is first solved using the conjugate gradient method. Once a solution is obtained, the tangential problem can be then solved, where the Coulomb friction law is applied as a bound to the shear distribution [47]. As a result, the distributions of the static normal pressure, the initial gap, and the contact stiffness for the contact interface can be obtained [30,47,48] and used for the nonlinear dynamic analysis. It was worth noting that the contact stiffness for either smooth or rough surfaces can be obtained from the semi-analytical solver using the following steps [52]: (1) Solve the normal contact problem for several normal loads around the given overall normal load; (2) Interpolate the normal indentation curve for each dynamical contact element where the slope of that curve gives the normal contact stiffness that defines for each dynamical contact element; (3) Solve the tangential problem for small values of tangential load (force or displacement) where the entire contact area remains in stick condition. This gives a portion of the linear part of the frictional hysteresis loop, from which the tangential contact stiffness can be extracted for each dynamical contact element.

2.3. Nonlinear dynamical analysis

The distributions of contact interface parameters from the semi-analytic solver are then associated with each 3D node to node contact element that discretized on the friction interface in the macro dynamic FE model [7]. Four parameters of each contact element, namely the normal load, the initial gap, and the normal and tangential contact stiffness, are defined, based on the previously refined contact analysis, at the beginning of the nonlinear dynamic analysis. The up-scaling of these distributions to the coarser FE model follows Newton's third law to ensure that the forces and moments at the contact interface are the same across different interface geometry scales. This expansion of highly detailed semi-analytic solver data to the much coarser FE model, significantly simplifies the modeling of a mesoscale interface geometry while maintaining high accuracy of the actual geometry, since it allows considering strong local interface geometry effects on the pressure distribution characteristic of the non-smooth contact.

A nonlinear dynamic analysis, based on the harmonic balance methods, is performed using the macro-scale FE model with the input contact loads from the semi-analytic solver. The methodology for the nonlinear dynamical analysis is based on damped nonlinear modal analysis, adaptive reduced order modeling and extended-energy balance method [33,35,39]. A brief introduction will be given here for completeness.

2.3.1. Equation of motion

The equation of motion for the dynamic analysis is shown in Eq. (4):

$$\mathbf{M}\,\ddot{u}(t) + \mathbf{C}\,\dot{u}(t) + \mathbf{K}\,u(t) + \mathrm{F}_{nl}(u(t)) = \mathrm{F}_e(\gamma,\varphi,\Omega,t) \tag{4}$$

where $u(t)$ is the structural displacement; F_e is the periodic excitation force; F_{nl} is the nonlinear contact friction force; Ω is the excitation frequency; γ is the excitation forcing level; φ is the absolute phase of the excitation force; and $\mathbf{M}$, $\mathbf{C}$ and $\mathbf{K}$ are mass, viscous damping and stiffness matrix respectively.

2.3.2. Contact friction modeling

The contact friction model used in the FE model is based on a 3D node-to-node element, which incorporates two coupled tangential Jenkins elements to describe the slip and stick motions in the in-plane directions, and a normal spring to describe the transition of variable normal load and separation conditions. Fig. 2(a) shows the used contact element, where k_n and k_t are the normalized normal and tangential contact stiffness (N/mm^3), and μ is the friction coefficient. The pre-defined normal load N_0 and the gap defines the initial contact condition for each element. $x(t)$, $y(t)$, and $z(t)$ are the resulting relative tangential and normal displacements between two matching contact nodes in the local coordinate system of the element. Fig. 2(b) shows a comparison of numerical hysteresis loops from this 3D contact friction element and experimental one from [53]. In this study, the pre-defined normal load, the gap, the normal and tangential contact stiffness of each contact friction element, are all obtained from the semi-analytical solver. This 3D contact friction is then used to evaluate the normal and tangential contact force $F_{nl}(u(t))$ for each contact element as shown in Eq. (4).

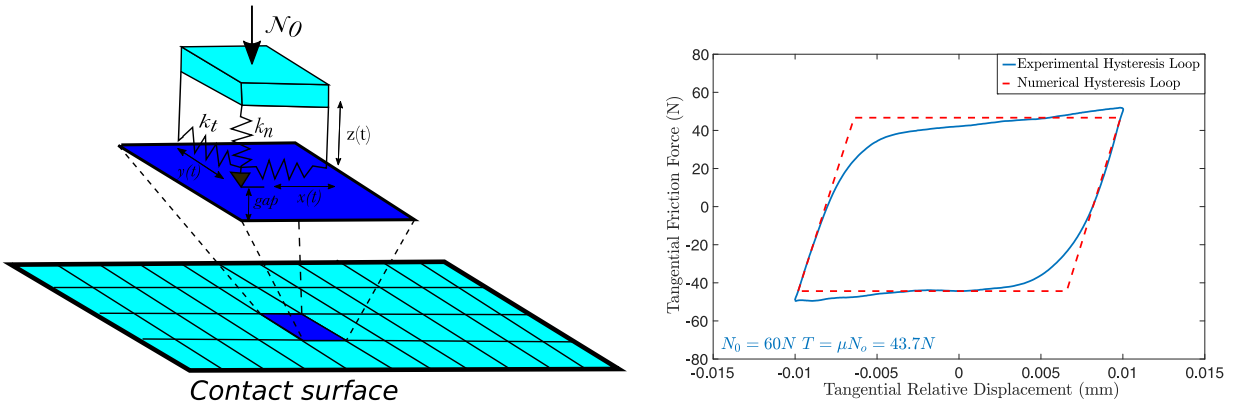

Fig. 2. (a) 3D node-to-node element [54] (b) Hysteresis loop.

2.3.3. Reduced order modeling

An adaptive reduced-order method is used to reduce the size of the macro-scale FE model. The fundamental formulation will be briefly shown here, but for more detail can be referred to [43,55]. The method is based on the linearized system, where the entire contact interface is assumed to be in a stuck condition. An internal variable Δp is introduced to the equation of the motion to take the slipping or separation condition into account. The modified equation of motion can be written as:

$$\begin{bmatrix} \mathbf{M} & \mathbf{0} \\ \mathbf{0} & \mathbf{0} \end{bmatrix} \begin{bmatrix} \ddot{u} \\ \Delta\ddot{p} \end{bmatrix} + \begin{bmatrix} \mathbf{C} & \mathbf{0} \\ \mathbf{0} & \mathbf{0} \end{bmatrix} \begin{bmatrix} \dot{u} \\ \Delta\dot{p} \end{bmatrix} + \begin{bmatrix} \mathbf{K}_L & \mathbf{BK_J} \\ (\mathbf{BK_J})^T & \mathbf{K_J} \end{bmatrix} \begin{bmatrix} u \\ \Delta p \end{bmatrix} = \begin{bmatrix} \mathrm{F}_e \\ \mathrm{F}_{nl} \end{bmatrix} \tag{5}$$

where the $\mathbf{K}_L(k_t, k_n)$ is the linearized stiffness matrix, $\mathbf{K_J}$ is the linear joint stiffness matrix associated with the DOFs at the contact interface, and $\mathbf{B}$ is the Boolean matrix to transform the joint matrix to the global system matrix. The adaptive reduced order model can then be constructed through two constitutive reductions. The first reduction is carried out using the vibration modes of the linearized system $\boldsymbol{\phi}$ and a full set of static constraint modes $\boldsymbol{\psi}$ that are associated with the nonlinear DOFs on the contact friction interfaces. The second reduction removes the static modes associated with constantly stuck contact nodes from $\boldsymbol{\psi}$ since these modes are redundant on the reduced basis as the motion of the stuck nodes is already represented by the linearized dynamic modes. The transformation matrix for the second reduction can be expressed as:

$$q_0 = \begin{bmatrix} u \\ \Delta p \end{bmatrix} = \underbrace{\begin{bmatrix} \boldsymbol{\phi} & \boldsymbol{\psi} \\ \mathbf{0} & \mathbf{I} \end{bmatrix} \begin{bmatrix} \mathbf{I} & \mathbf{0} \\ \mathbf{0} & \mathbf{B}_p \end{bmatrix}}_{\boldsymbol{\Phi}} \begin{bmatrix} \eta \\ \Delta p_R \end{bmatrix} \tag{6}$$

$$\mathbf{M_R} = \boldsymbol{\Phi}^T \mathbf{M_G} \boldsymbol{\Phi}, \mathbf{K_R} = \boldsymbol{\Phi}^T \mathbf{K_G} \boldsymbol{\Phi}, \mathbf{C_R} = \boldsymbol{\Phi}^T \mathbf{C_G} \boldsymbol{\Phi} \tag{7}$$

where η are the modal participation factors of the selected dynamic modes, $\boldsymbol{\phi}$ are the dynamic modes, and $\boldsymbol{\psi}$ is the full set of static constraint modes. Δp_R is the non-zero part of Δp and $\mathbf{B}_p$ is the Boolean matrix that helps to identify the non-zero part of Δp with an additional simulation to check the contact condition of the last converged solution, and finally $\boldsymbol{\Phi}$ is the transformation matrix for the adaptive reduced order model. The size of $\boldsymbol{\Phi}$ depends on the contact condition of the contact nodes. This adaptive ROM is highly effective for interfaces with a large number of stuck nodes, which is often the case for bladed disk connections, while contacts where all nodes slide during a vibration cycle would be less effective. $\mathbf{M_G}$, $\mathbf{K_G}$ and $\mathbf{C_G}$ are extended mass, stiffness and damping matrix from the Eq. (5). Using the adaptive modal projection matrix $\boldsymbol{\Phi}$, the reduced mass matrix $\mathbf{M_R}$, stiffness matrix $\mathbf{K_R}$ and damping matrix $\mathbf{C_R}$ can be computed via Eq. (7).

2.3.4. Damped nonlinear modal analysis

The damped nonlinear modal analysis, based on EPMC [33], is used to obtain resonance frequencies and damping ratios of the nonlinear dynamical system. As shown in Eqs. (8) and (9), an artificial mass proportional modal damping $\mathbf{C_a}$ is added to make the motion of the system periodic [33]. Since the modal properties of the dNNM are dependent on the level of energy within the system, the modal amplitude α is used to represent the system energy. $\omega_o(\alpha)$ and $\eta(\alpha)$ are the amplitude-dependent resonance frequency and the artificial mass proportional modal damping of this dissipative system. This additional term is used to balance the dissipation of the frictional energy from the nonlinear contact interface with the linear damping terms in the modified Eq. (5). Using the adaptive reduced order models from above, the equation of motion can be rewritten as Eq. (9):

$$\mathbf{C_a} = -2\omega_o(\alpha)\eta(\alpha)\mathbf{M_R} \tag{8}$$

$$\alpha(\mathbf{M_R}\,\ddot{q}_0(\alpha,t) + \mathbf{C_a}\,\dot{q}_0(\alpha,t) + \mathbf{C_R}\,\dot{q}_0(\alpha,t) + \mathbf{K_R}\,q_0(\alpha,t)) + \mathrm{F}_{nl}^R(\boldsymbol{\Phi}(\alpha q_0(\alpha,t))) = 0 \tag{9}$$

2.3.5. Forced resonant response prediction

To enable a direct comparison to experimental results, the prediction of forced resonance response can be obtained. Since dNNMs are essentially a series of resonant solutions, the forced response at different excitation levels and locations can be interpolated from the dNNMs via the Extended-Energy Balance Method (E-EBM) [38]. Under the assumption of small forcing amplitudes and damping, the solution between forced resonance and dNNM is nearly identical. Here the forced resonant solution q_f is assumed to be equivalent to the dNNM with a certain level of modal amplitude $q = \alpha \cdot q_0(\alpha)$ under the condition that the excitation frequency Ω coincides with the modal resonance frequency ω_o. The shared solutions between the dNNM and forced response level will be noted as χ.

$$\chi = q \approx q_f, \text{when } \Omega = \omega_o(\alpha) \tag{10}$$

$$E_d = \int_0^{2\pi/\omega_o(\alpha)} (2\omega_o(\alpha)\eta(\alpha)\mathbf{M}_R) \cdot \dot{\chi} \cdot \dot{\chi} dt \tag{11}$$

$$E_f(\gamma, \varphi) = \int_0^{2\pi/\Omega} \mathrm{F}_e(\gamma, \varphi, \Omega, t) \cdot \dot{\chi} dt \tag{12}$$

$E_f(\gamma, \varphi)$ (the external excitation energy) can be integrated as shown in Eq. (12). It varies with the applied forcing level γ and the forcing phase φ. Similarly, E_d, the internal dissipated energy, can be obtained through numerical integration of the artificial damping force in Eq. (8), where the displacement over one vibration period is shown in Eq. (11). One single intersection will occur at the maximum position between the curve of E_f (E_f against φ) and the constant E_d, which can help to determine the value of γ and φ for the solution. The corresponding forced resonance amplitude can be found for each value of a modal amplitude α at the selected excitation position, leading to a complete frequency response function.

2.3.6. Harmonic balance methods

The Harmonic Balance Method (HBM) is used to evaluate the steady-state dynamic response of large-scale nonlinear systems. The principle of this method is to discretize the displacement $q(t)$ in the frequency domain using a truncated Fourier series:

$$q(t) = \tilde{Q}_0 + \sum_{i=1}^{n_h} (\tilde{Q}_i^c \cos m_i\omega_o t + \tilde{Q}_i^s \sin m_i\omega_o t) \tag{13}$$

where $\tilde{Q}_0$ is the zeroth harmonic coefficient; $\tilde{Q}_i^{c,s}$ are the cosine and sine coefficients for the ith harmonic; n_h is number of harmonics to be included in the analysis; and ω_o is the forcing frequency. The equation of motion is transformed into a set of algebraic equations including the Fourier series. To solve these nonlinear equations, a Newton–Raphson solver, an Alternating Frequency Time (AFT) procedure, and a continuation technique [3,43,56] are used. The AFT technique thereby evaluates the nonlinear force in the time domain and transfers the results back to the frequency domain. The detailed implementation of HBM with the adaptive reduced order model method and nonlinear modal analysis can be found in [39]. In this study, to track the nonlinear dynamic response, a continuation technique that tracks the modal amplitude α has been implemented. A predictor–corrector procedure [56] based on the Secant method is employed for the predictor while the arc-length method is used for the corrector. Two additional constraints are applied to the damped nonlinear modal analysis which are the phase constraint and mass normalization [33].

In summary, the proposed multi-scale framework integrates advanced nonlinear modal analysis coupled with adaptive reduced-order modeling techniques for the first time. It will be used in this study to investigate the effect of mesoscale features on a typical engineering jointed structures and evaluate the effectiveness of the proposed framework.

3. Case study

3.1. Dogbone test rig and FE model

The case study is based on an assembled model that represents an available blade root test rig for fan blade systems at the Dynamics Group at Imperial College London [46]. Fig. 3(a) shows the so-called dog bone test rig setup to measure blade root damping. It includes two major components: (i) a set of identical solid root-block disks that contain the root slots; (ii) a single “Dogbone” with matching blade roots on both ends.

The disks can accommodate up to 16 root designs, where five adjacent sides have currently been machined to house various blade root designs for dovetail joints and fir-tree roots. A near-point contact with a hardened U-shaped hook is used to suspend the disks in a tensile test machine. Fig. 3(b) shows a typical dovetail joint, which is used in fan blade disks, and which is the focus of this case study. The FE model representing the overall test rig can be seen in Fig. 3(c) and a detailed view is shown in Fig. 3(d). The mesh was obtained with Hypermesh and a large effort was made to provide very detailed matching meshes at the four contact interfaces (two for the top root and two for the bottom root). The size of each contact friction interface is approximately 18 mm x 1.6 mm which is discretized via 28 nonlinear elements (involving 40 contact nodes) in the macro-scale FE model. For four contact interfaces in the Dogbone test rig, there are in total 160 contact nodes namely 480 nonlinear DOFs. The whole test rig is made up of a total of 58,592 quadratic hexahedral elements. To reduce the computational cost, the disks are simplified as a cyclic sector as shown in Fig. 7(a). The test rig is made of steel with a Young’s modulus of 200 GPa and a density of 7.84 g/cm3.

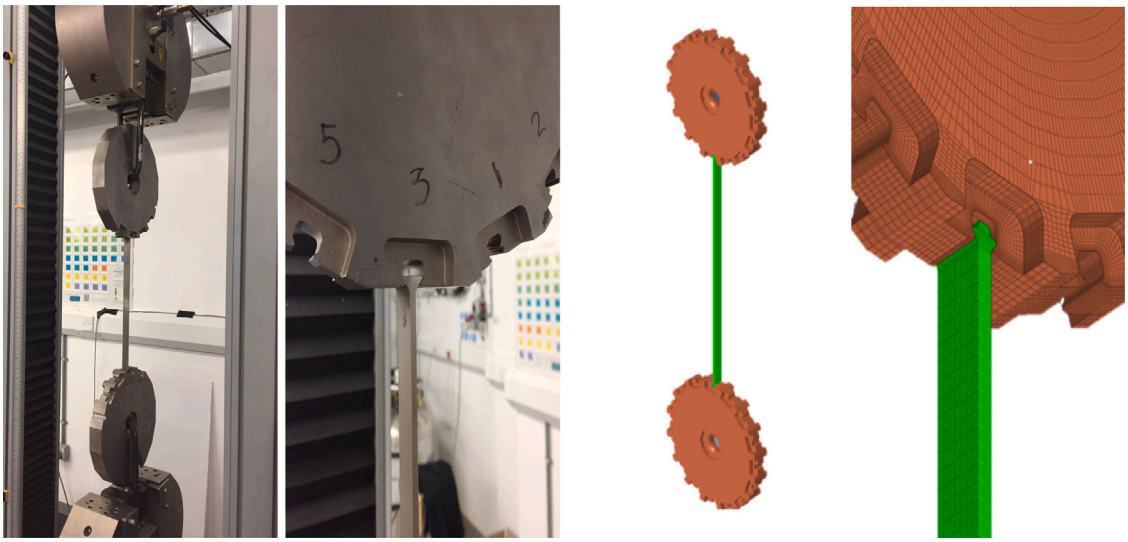

Fig. 3. (a) Dogbone Test rig setup; (b) The dovetail root; (c) FE model of Dogbone rig; (d) FE model of the dovetail root.

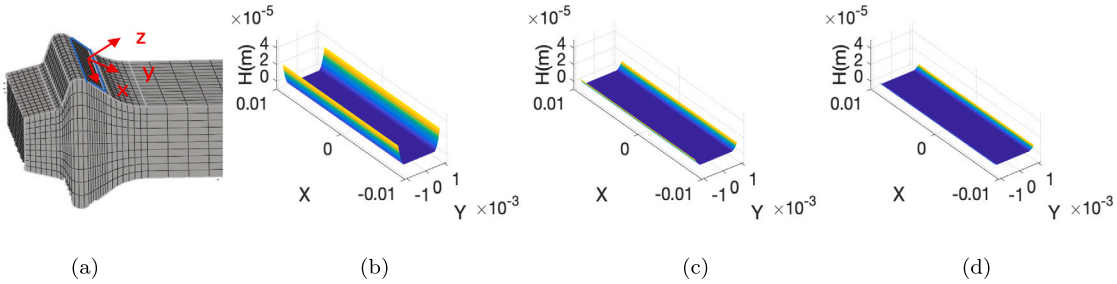

Fig. 4. (a) Dogbone friction interface; (b) R=2 mm; (c) R=6 mm; (d) R=10 mm .

3.2. Friction interface geometry

In this study, the impact of different mesoscale interface geometry design parameters (contact edge radius and interface topology) will be investigated, together with the influence of some of the key friction contact parameters for a fan blade system.

3.2.1. Interface edge radius and topology

Fig. 4(a) shows one of the four contact friction interfaces in the Dogbone root. Due to the symmetry of the setup, it will be assumed that all four interfaces load up in an identical manner. The edge radius of the contact interface is regarded as an important parameter that not only impacts the maximum hoop stress and fatigue life of the dovetail root design in fan blade systems [57], but also influences the nonlinear dynamic response due to a concentration of contact pressure close to the edges. Fig. 4(b), 4(c) and 4(d) show three friction interface geometries with different edge radii (R=2 mm, R=6 mm and R=10 mm) on the bone itself that will be considered in this study. It can be seen that, with the increase of the edge radius, the curvature on the edge becomes much less significant.

The second mesoscale interface feature of interest is the actual interface shape. Fig. 5 shows the three different interface profiles that have been investigated: (a) the Y-wise bump, (b) the Center bump, and (c) the Y-wise Concave respectively. These profiles can mitigate the maximum hoop stress on the interface [58] and are expected to significantly affect the dynamic response [24] of the Dogbone. Besides investigating the effect of the different shapes, a parametric study with different levels of bump height will be performed for the center bump in Fig. 5(b). The results will be referenced to a flat-on-flat contact interface, which represents the nominal case. To represent these mesoscale friction interface geometry, 250 × 125 meshing points are used for refined contact analysis using the semi-analytic solver.

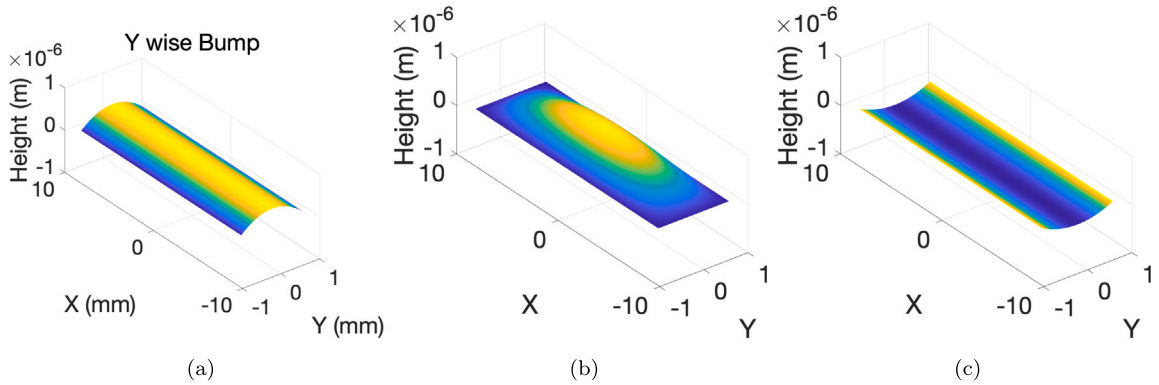

Fig. 5. Interface profiles: (a) Y Bump; (b) Center Bump; (c) Y wise Concave.

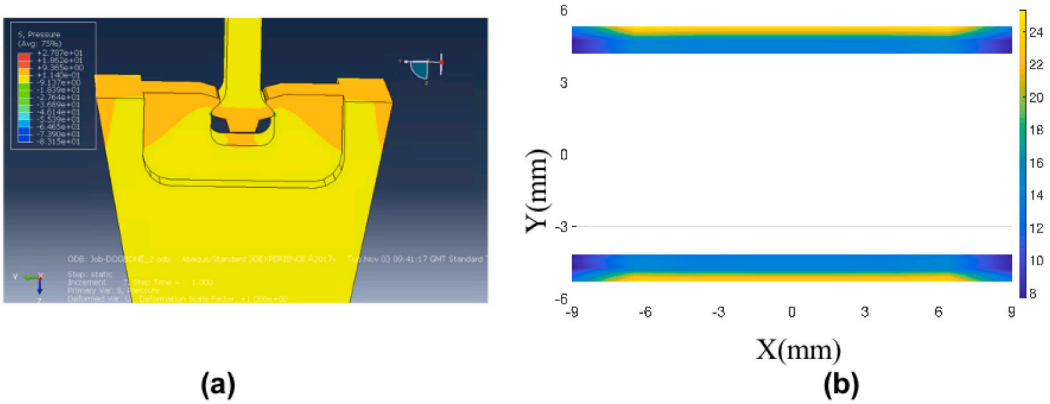

Fig. 6. (a) Pressure distribution in Dogbone rig dovetail root; (b) Contact pressure on the friction interfaces.

3.2.2. Interface contact parameters

Different levels of the pre-loading applied to the Dogbone rig will be studied. For a fan blade system, the level of the pre-loading will be dependent on the centrifugal loading due to the rotation speed. In this study, four different pre-loading levels, including 500 N, 1000 N, 1500 N, and 2500 N will be considered. These pre-loading levels will be applied for nonlinear static analysis by pulling one disk while clamping the other one using the developed FE model. The effect of the Coefficient of Friction (CoF) will also be investigated since fan blade roots are often dry film lubricated to mitigate the effects of fretting wear [59–61]. Based on the previous experimental data [59], two CoF will be studied in this paper, which is 0.4 for the dry lubricated surface and 0.8 for the surface without coating.

4. Results

This section presents the numerical results using the proposed multi-scale approach for an analysis of the Dogbone rig. The effects of the interface geometry and contact parameters on the nonlinear dynamic response will be discussed.

4.1. Nonlinear static analysis

Fig. 6 a shows the stress distribution from nonlinear static analysis of the Dogbone test rig, which was performed using ABAQUS. Surface-to-surface hard contact is used on the flat contact interfaces. The end of the top disk sector is fully fixed while a pulling loading of 1000 N is applied at the opposite side to the bottom disk. The resulting distribution of the normal pressure on the two opposing lobes of the root is shown in Fig. 6b. Due to a predicted small deformation of the dovetail root, leading to an opening of the root slot, the normal contact pressure is concentrated at the lower part of the interface but all of the interfaces stay in contact with no opening of a gap appearing. Due to the symmetry of the test rig and loading conditions, the pressure distribution on the other two doge bone lobes is the same.

The pressure distributions from the quasi-static analysis are summed up to obtain an equivalent force and moment vector at the center of each contact interface, which will be used for the refined contact analysis in the semi-analytic solver. It is worth noting that the obtained contact force for each interface can be affected by the selection of the penalty parameter. The choice of

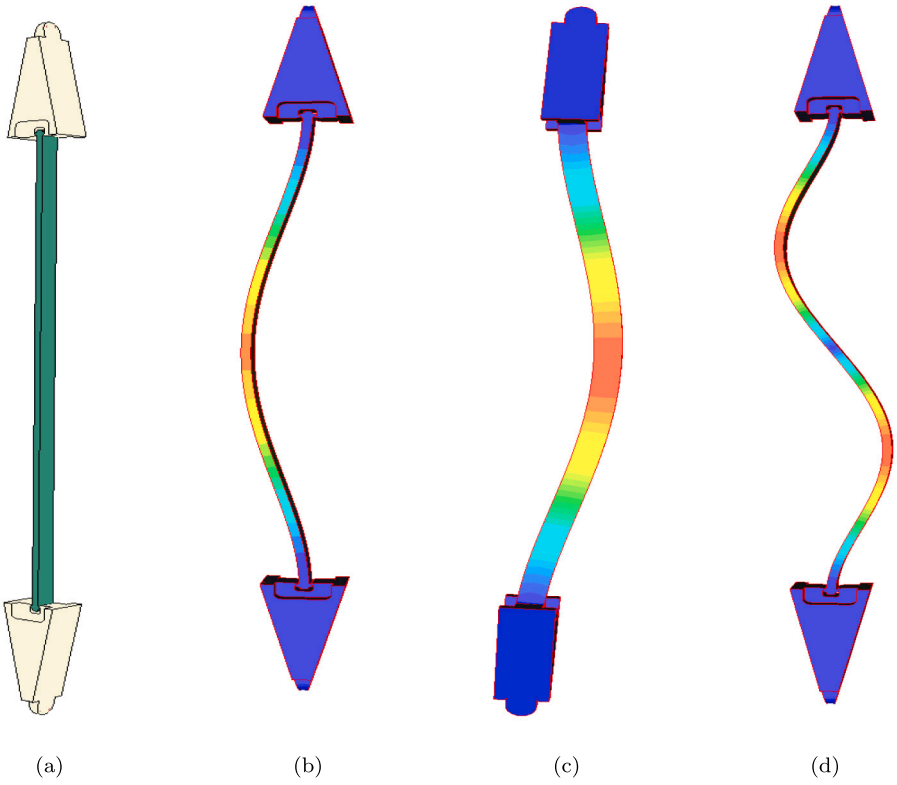

Fig. 7. (a) Reduced FE model; (b) First mode; (c) Second mode; (d) Third mode.

penalty parameters is mainly dependent on the criteria defined by the user. In this study, the contact stiffness (one of key penalty parameters) that relates contact force to the penetration distance for the hard contact was chosen automatically by the solver to optimize the time increment. Such an approach has also been used in previous studies for the design of friction dampers [6,17], where it showed to lead to good results.

4.2. Linear modal analysis

Fig. 7(b), 7(c) and 7(d) show the first three bending modes of the test rig FE model from a linear modal analysis, where the contact interfaces were fully glued. The first out-of-plane mode will thereby be the focus of this study.

4.3. Effects of the interface edge radius

The overall contact load obtained from the nonlinear quasi-static analysis is applied to the semi-analytic contact solver. The contact interface is discretized into a much finer mesh (250 × 125 meshing points) so that different mesoscale profiles can be well represented. The computation of the refined contact analysis for each profile only takes around 20 s using the semi-analytical solver. Fig. 8 shows the resulting contact pressure distribution at the edge of the interface for different values of the edge radii. With the increase of the edge radius from 0 mm (no radius) to 10 mm, the maximum contact pressure at the edge of the interface is reduced significantly from 250 MPa to 140 Mpa. As the radius increases, the pressure distribution starts to move slightly toward the center of the contact surface, leading to a more uniform pressure distribution and a smaller maximum contact stress. The detailed pressure distribution results are being expanded out to the 3D FE model to allow a nonlinear dynamic analysis. The gap on the contact interface for different levels of radii considered in this study is zero.

Fig. 9 shows the influence of the edge radius on the nonlinear dynamical response, in terms of the resonance frequency and friction loss factor η where the damping is mainly contributed from the friction interface. The equivalent force is evaluated using the E-EBM by applying the periodic forcing in the middle of the bone and in the out-of-plane direction. It can be seen that with an increase in the force the resonance frequencies drop by approximately 5% for all radii, while the damping initially increases before it starts to drop again. The increase in damping is thereby attributed to an increase of sliding elements at larger amplitudes, while the decrease is mainly due to the macro-slip at the contact interface where the interface lost the contact. Fig. 10 shows the energy dissipation distribution across the contact interface at different excitation levels when the edge radius is 2 mm. With the increase of the force level, the energy dissipation gradually grows from the center of the contact outwards.

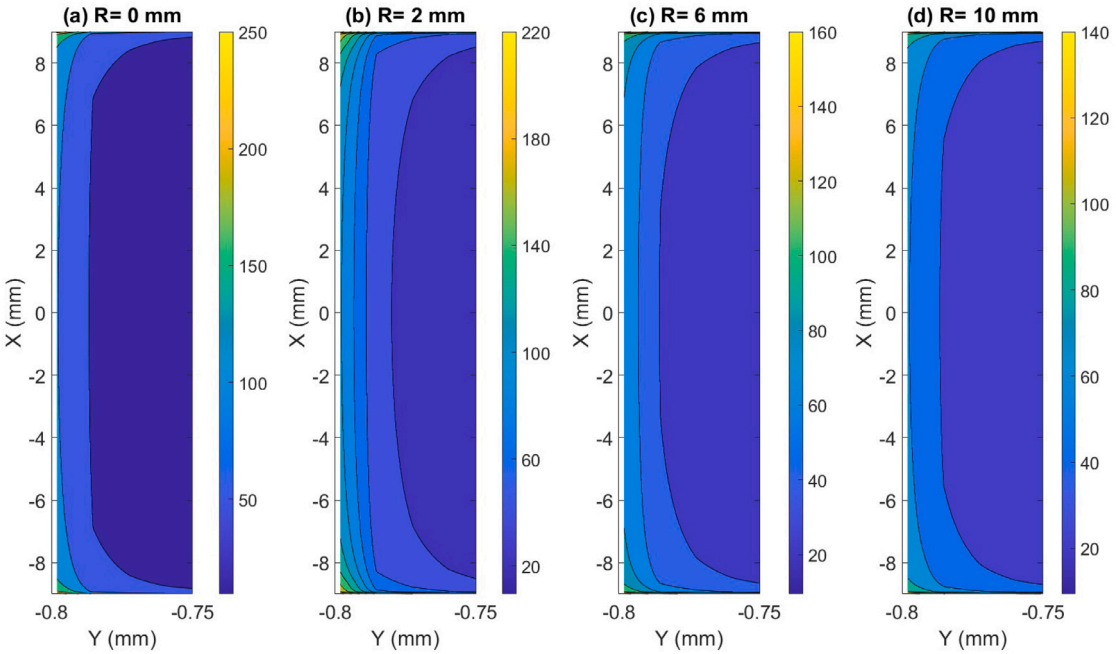

Fig. 8. Normal contact pressure from refined contact analysis (a) R=0 mm; (b) R=2 mm; (c) R=6 mm; (d) R=10 mm;.

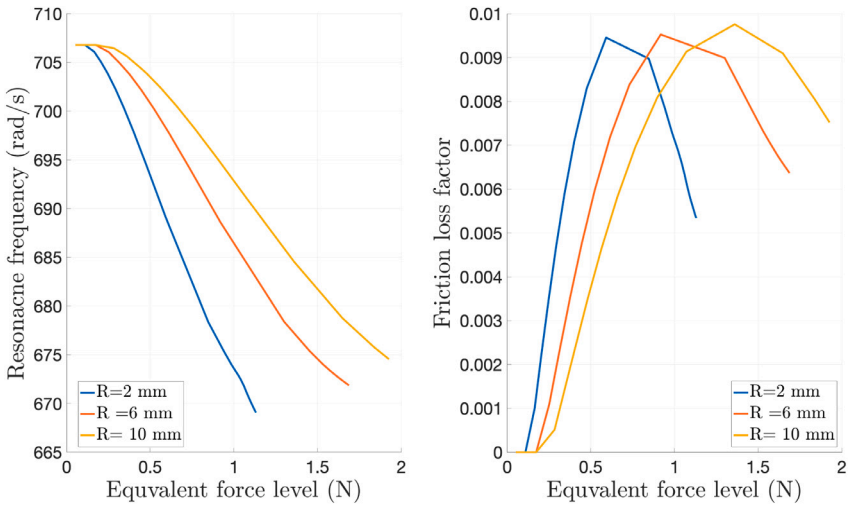

Fig. 9. (a) Resonance frequency (b) Friction loss factor.

Comparing the effects of the three radii, it can be seen that the rate of increase/decrease in both friction loss factor and resonance frequency has been reduced by the increasing edge radius, and hence that the system becomes less nonlinear as the edge radii increase. This is in agreement with the contact pressures in Fig. 8, where it could be seen that the contact pressure of the inner contact area increases with the edge radius leading to a higher sliding limit.

4.4. Effects of interface profiles

Fig. 11 shows the normal pressure distribution of various interface profiles as described in Fig. 5. Not surprisingly the pressure is concentrated along the middle of the interface for the Y-wise bump profile, in the center for the central bump profile, and along the edge for the Y-wise concave profile. The gap distribution for the central bump configuration, obtained from the refined contact analysis, is shown in Fig. 12. It gives an example of how the gap distribution is obtained for the central bump profile through the initial gap and the deformation distribution on the contact interface. The initial gap refers to the space between two contact

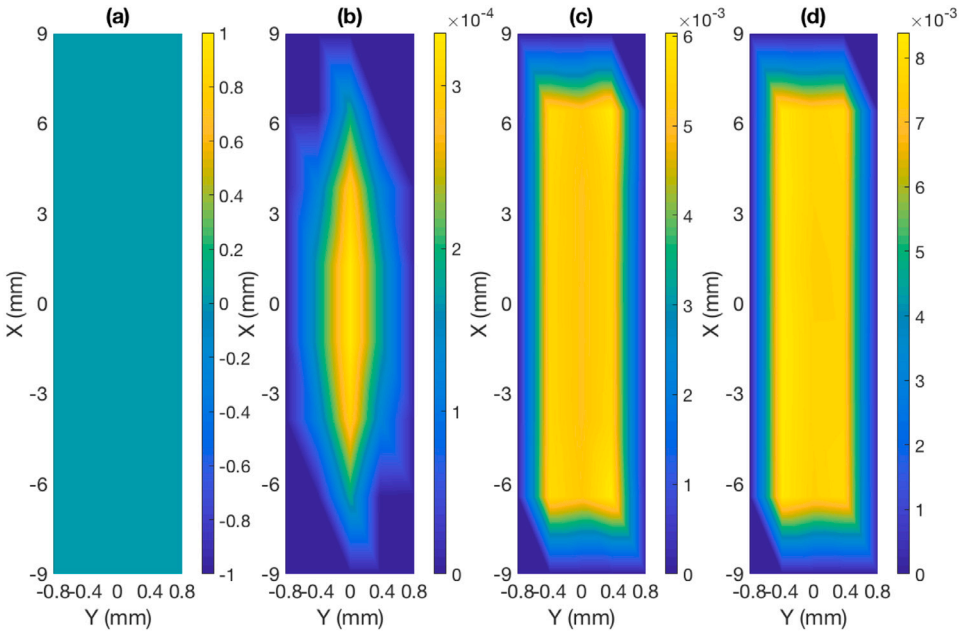

Fig. 10. Energy dissipation on the friction interface with a edge radius of 2 mm with increasing force levels (a) 0.05 N (b) 0.2 N (c) 0.6 N (d) 0.8 N.

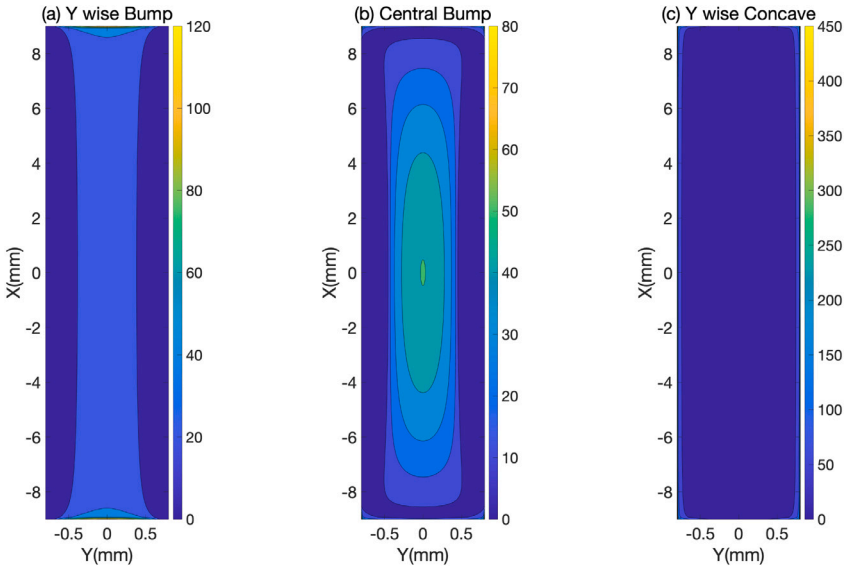

Fig. 11. Normal contact pressure from refined contact analysis (a) Y-wise Bump; (b) Center Bump; (c) Y-wise Concave.

interfaces without any applied contact loads. The deformation distribution refers to the deformation of the interface after the contact load is applied. The difference between the initial gap and the deformation is therefore the gap distribution.

Fig. 13 shows the resonance frequencies and friction loss factors of all three profiles. Once more the resonance frequencies decrease with the force level while the loss factors increase due to the increasing slipping area on the friction interface. Interestingly the global trends for these profiles are quite similar, given the strong variations in the normal load distribution, but the gradients of the curves are somewhat different. For the flat and the Y concave profile, both resonance frequencies, and damping change very rapidly once sliding occurs since their normal pressure is localized at the interface edges and once they break loose, nothing is stopping the contact from sliding. The Y and C bumps change much more gradually as their contact pressure distribution is covering a much wider contact zone. The initial resonance frequencies for the Y and C bumps are lower than those of the Y concave and flat interface. This can be attributed to a reduction in the overall interface stiffness since the bumped profiles lead to gaps or much lower pressures on the edge of the contact interface. The loss factors of these four profiles are also slightly different, especially at low

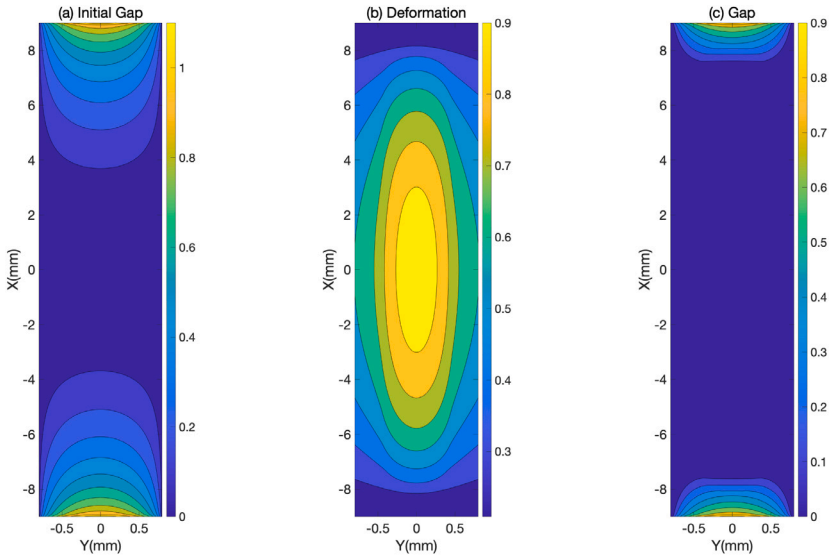

Fig. 12. An example of the gap distribution of a central Bump.

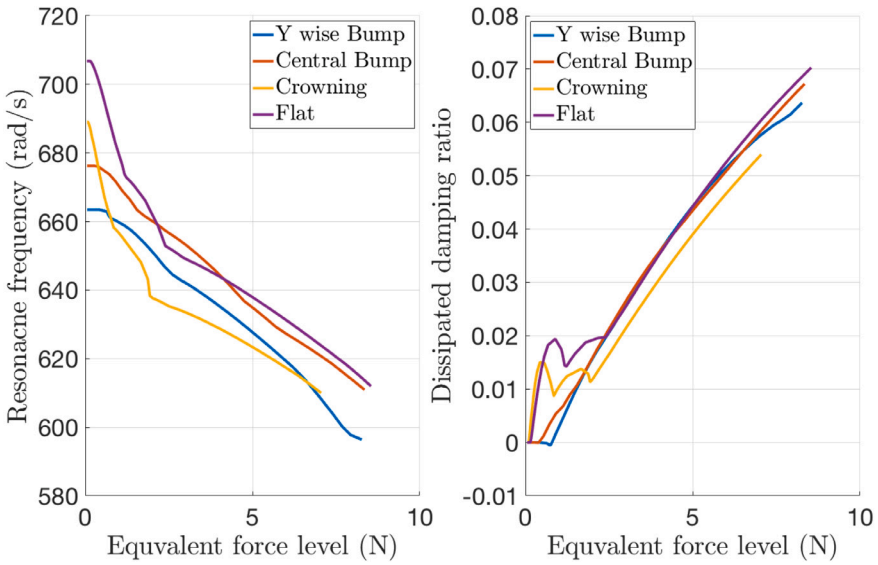

Fig. 13. The comparison of three different interface geometries (a) Resonance frequency (b) Friction loss factor.

excitation levels. The bumpy interfaces show a steady growth of damping while the other two show an initial steep and unsteady increase in excitation levels due to a much more localized pressure distribution at the contact interface. Overall, with a different mesoscale friction interface geometry, the resonance frequency drops by up to 5.7% while the growth of the friction loss factor can up by an order of magnitude indicating that different mesoscale interface profiles may be used to design the nonlinear dynamic response. The distribution of energy dissipation for these four contact interface profiles at the excitation level of 2N is shown in Fig. 14. The energy distribution is consistent with the pressure distribution of these four interface profiles as shown in Fig. 11.

4.5. Effect of the level of interface bump height

Figs. 15 and 16 show the variation of interface pressure and gap distribution with the increase of the bump height for the Central bump interface from 40 μm to 140 μm. While the lowest bump provides a relatively even distribution across the entire interface, each increase leads to a more concentrated pressure in the center. The maximum pressure increases from 25 Mpa to 40 Mpa as the bump height increases. Fig. 16 shows that the contact area decreases with an increasing bump height. Applying the obtained pressure distributions and gaps to the FE model allows to compute the nonlinear dynamic response.

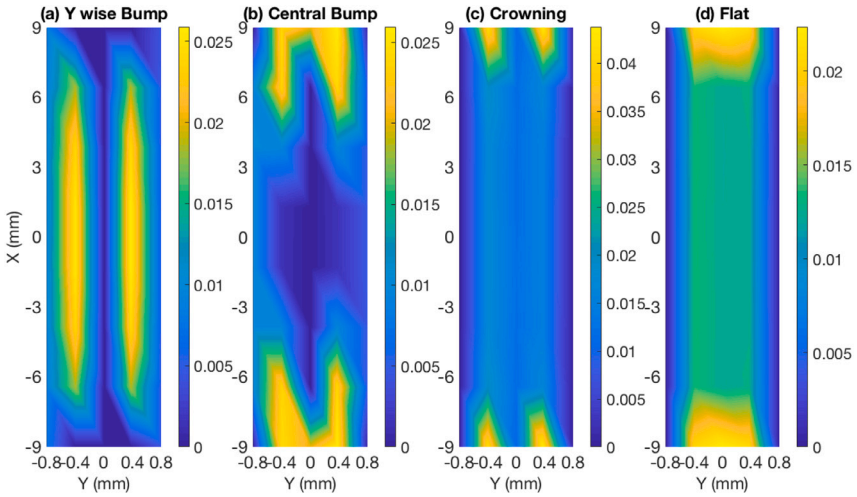

Fig. 14. The comparison of Energy dissipation on three interface geometries.

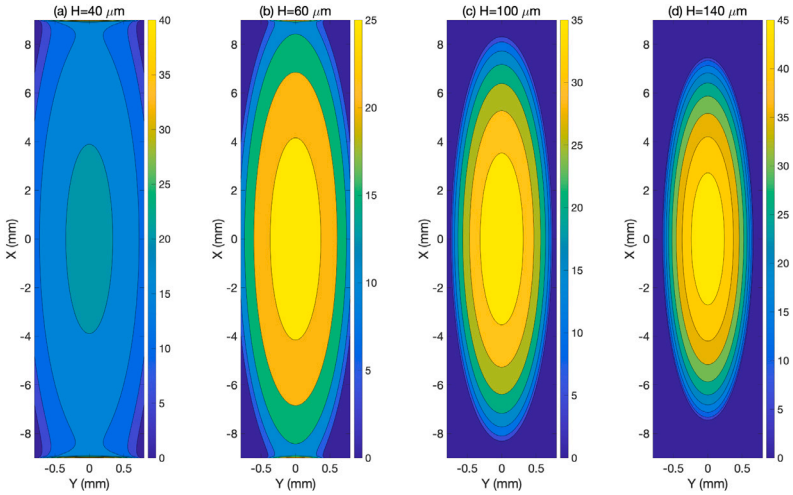

Fig. 15. The normal pressure of the Central Bump at diffident levels of bumpiness.

Fig. 17 shows the change of the nonlinear modal properties for the central bump with different heights. As the bump height increases, the linear resonance frequency reduces from 700 to 600 rad/s due to the reduction in the contact area. As the force level grows, the resonance frequency increases initially and then goes down a bit. The initial increase can be attributed to a closing of the initial gaps as vibration occurs, leading to an increase of interface stiffness. The decrease at higher force levels is due to the onset of slip at the interface. The resonance frequency of the interface profile with low bump heights are more sensitive to large force levels, while the interface with higher bumps behave more linearly at large amplitudes but are quite sensitive to low amplitude excitation. The interfaces with higher bumps lead to smaller damping at high amplitudes, while they appear to generate a bit more damping at low amplitudes.

4.6. Effects of contact parameters

The effects of the pre-load and the interface COF on the nonlinear modal properties has also been investigated for the Central bump case. The height of the central bump is 60 um. Fig. 18 shows the resulting contact pressure distribution for four different pre-loading levels with a CoF of 0.4. As expected, the contact area and maximum contact pressure increase with the pre-loading levels. It is worth noting that once the contact pressure reaches the edges, a significant jump in the maximum contact pressure can be observed due to the singularity at the edge. Figs. 18b and 18e show a comparison of the pressure distribution of the central bump for CoF of 0.4 and 0.8 under the same pre-load of 1000 N. Both pressure profiles share the similar maximum contact pressure and distribution. However, for a higher CoF, the distribution of the contact pressure is more centralized. Fig. 19 shows the resulting gap

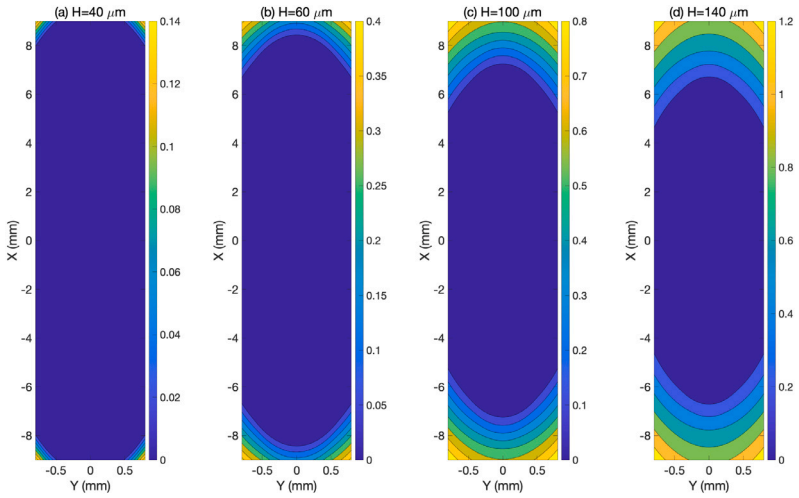

Fig. 16. The gap distribution of the Central Bump at diffident levels of bumpiness.

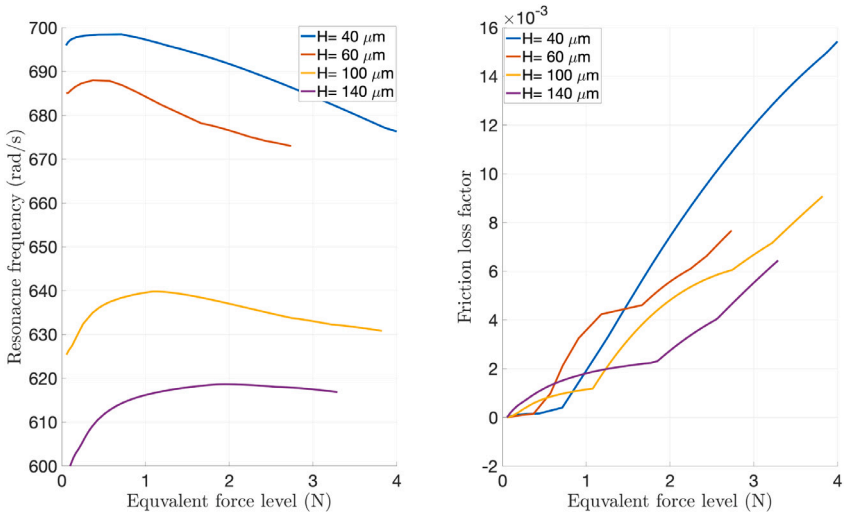

Fig. 17. Nonlinear dynamics of the Central Bump at diffident levels of bumpiness.

distributions of the center bump at the different pre-loading levels and CoFs. As expected, the gap area decreases with the increase of pre-load. For the higher CoF of 0.8 shown in Fig. 19e, it can be seen that the gap area is slightly larger than for the contact interface with a CoF of 0.4 shown in Fig. 19b.

Fig. 20 shows the comparison of the nonlinear modal properties of the central bump at four pre-loading levels and for two different CoF. The solid line represents the interface with a CoF of 0.4 while the dashed line represents the interface with a CoF of 0.8. The normal load has a significant impact on the resonance frequencies of the system, leading to a nearly 100 rad/s shift from the lowest to the highest load. Similar to the increase in bump height, the initial resonance frequencies increase due to the increasing deformation that close the gap on the edges but then tend to drop again as the interface starts to slip more so that the friction damping effect dominates. The resonance frequency is not too much affected by the CoF change, indicating that a bump profile is relatively robust in terms of frequencies. Not surprisingly the friction loss factors reduce significantly with an increasing pre-load since a higher load leads to more stuck elements and hence less energy dissipation. The CoF shows a significant effect on the damping behavior, where the higher CoF almost maintains a stuck condition throughout the investigated range, while the lower friction coefficient shows much more damping.

These obtained results can be compared, in the first instance, to available measurement results in the literature [24] obtained from a very similar test setup. The comparison shows that the results from the simulations in this study share very similar trends in the loss factor curves for both flat-to-flat friction interfaces and crowning bump interfaces at different pre-loading levels where the friction loss factor changes abruptly for the flat-on-flat surface while the transition is more smooth for the crowning bumped surface.

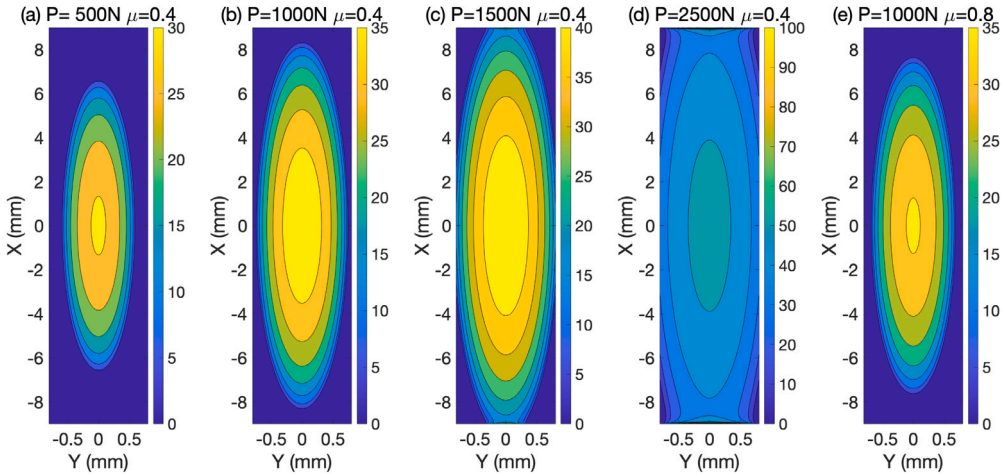

Fig. 18. Normal pressure of the Central Bump at diffident levels of Preloading and CoFs.

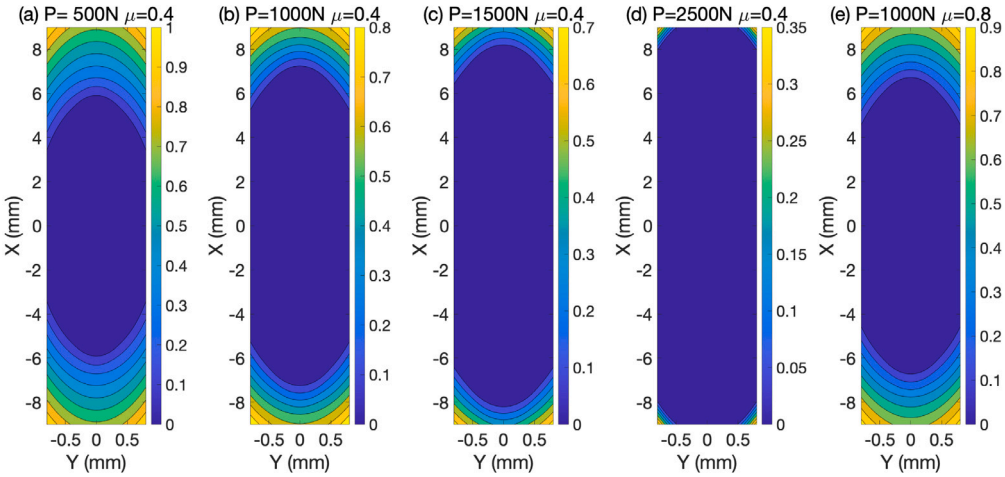

Fig. 19. Gap distribution of the Central Bump at diffident levels of Preloading and CoFs.

5. Conclusions

The objective of this study was to initially develop a computationally efficient framework that allows to assess influence of mesoscale friction interface geometries, such as waviness or edge radii, on the nonlinear dynamic response of large assembled structures through a multi-scale approach. The developed approach was then applied to a blade root test setup to highlight the impact of mesoscale parameters on the nonlinear dynamic response. The mesoscale friction interface model was effectively integrated into a macro-scale FE model for multi-scale analysis of the friction interface geometry. To further improve the efficiency of the multi-scale analysis, advanced nonlinear modal analysis, and an extended energy balance method were added to an existing framework.

A fan blade dovetail damping testing rig model was used as a case study. A nonlinear dynamic model of the system was created, following the developed framework and the effect of a series of different mesoscale interface geometries, such as surface bumps and edge radii, on the nonlinear modal properties were numerically investigated for the first time. Due to regular lubrication of such interfaces different contact parameters including pre-loading levels and the coefficient of friction were also simulated.

The results have demonstrated that the influence of mesoscale interface profiles on the damping and resonance frequencies can be quite significant. The edge radii can greatly change the contact stress on the friction interface, and significantly impact the nonlinear behavior of both friction loss factor and resonance frequencies. The height of a bumped profile can be used to influence the distribution of contact loads and area at the interface, significantly shifting the resonance frequencies and affecting the sensitivity of the damping toward the force levels. As expected a very strong dependency on the normal load levels was observed where higher loads lead to stiffer and more linear systems. A higher CoF was shown to make the resonance frequencies and damping ratios less sensitive to the forcing level.

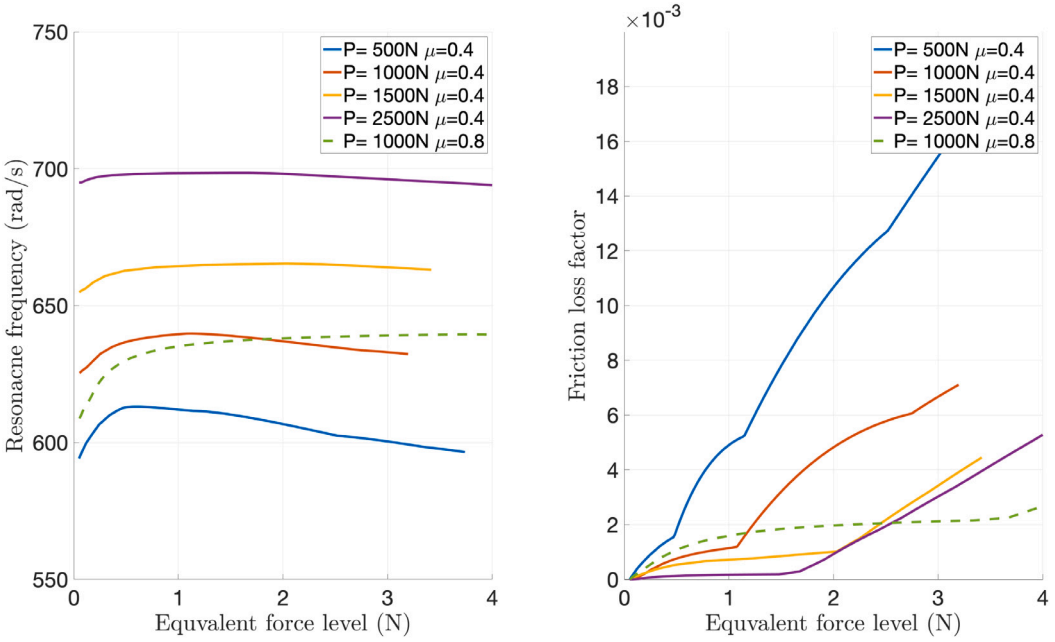

Fig. 20. Nonlinear dynamics of the Central Bump at diffident levels of bumpiness.

The study has shown that an accurate representation of the mesoscale interface geometry is highly recommended, since it can impact the observed nonlinear dynamic response significantly, and the current state of the art to model a flat-on-flat interface condition should not be considered accurate enough. In the future, a pre-optimized mesoscale friction interface geometry may be potentially used to improve the dynamic design of complex and nonlinear systems. The work opens a new research direction of the design of the friction interface for general friction involved mechanical systems.

CRediT authorship contribution statement

Jie Yuan: Conception and design of study, Methodology, Software, Analysis and/or interpretation of data, Writing – original draft, Funding acquisition. **Loic Salles:** Methodology, Writing – review & editing. **David Nowell:** Writing – review & editing. **Christoph Schwingshackl:** Conception and design of study, Analysis and/or interpretation of data, Writing – review & editing, Funding acquisition.

Declaration of competing interest

The authors declare that they have no known competing financial interests or personal relationships that could have appeared to influence the work reported in this paper.

Data availability

Data will be made available on request.

Acknowledgments

J. Yuan acknowledges the support of Small Research Grant from Royal Society of Edinburgh (RSE/1754). J. Yuan, L. Salles and C. Schwingshackl also acknowledges the funding from the EPSRC, UK through SYSDYMATS project WP3 (EP/R032793).

All authors approved the version of the manuscript to be published.

References

[1] C. Schwingshackl, E. Petrov, D. Ewins, Measured and estimated friction interface parameters in a nonlinear dynamic analysis, Mech. Syst. Signal Process. 28 (2012) 574–584, http://dx.doi.org/10.1016/j.ymssp.2011.10.005.

[2] R. Lacayo, L. Pesaresi, J. Groß, D. Fochler, J. Armand, L. Salles, C. Schwingshackl, M. Allen, M. Brake, Nonlinear modeling of structures with bolted joints: A comparison of two approaches based on a time-domain and frequency-domain solver, Mech. Syst. Signal Process. 114 (2019) 413–438, http://dx.doi.org/10.1016/j.ymssp.2018.05.033.

[3] M. Krack, L. Salles, F. Thouverez, Vibration prediction of bladed disks coupled by friction joints, Arch. Comput. Methods Eng. 24 (3) (2017) 589–636, http://dx.doi.org/10.1007/s11831-016-9183-2.

[4] Y. Sun, J. Yuan, L. Pesaresi, E. Denimal, L. Salles, Parametric study and uncertainty quantification of the nonlinear modal properties of frictional dampers, J. Vib. Acoust. 142 (5) (2020) 051102, http://dx.doi.org/10.1115/1.4046953.

[5] E. Denimal, C. Wong, L. Salles, L. Pesaresi, On the efficiency of a conical under-platform damper for turbines, in: Turbo Expo: Power for Land, Sea, and Air, Vol. 84232, American Society of Mechanical Engineers, 2020, http://dx.doi.org/10.1115/GT2020-14642, V011T30A012.

[6] Y. Sun, J. Yuan, E. Denimal, L. Salles, Nonlinear modal analysis of frictional ring damper for compressor blisk, Trans. ASME, J. Eng. Gas Turbines Power 143 (3) (2021) 031008, http://dx.doi.org/10.1115/1.4049761.

[7] Y. Sun, E. Denimal, J. Yuan, L. Salles, Geometric design of friction ring dampers in blisks using nonlinear modal analysis and Kriging surrogate model, Struct. Multidiscip. Optim. 65 (3) (2022) 1–25, http://dx.doi.org/10.1007/s00158-021-03093-w.

[8] M.R.W. Brake, J. Groß, R.M. Lacayo, L. Salles, C.W. Schwingshackl, P. Reuß, J. Armand, Reduced order modeling of nonlinear structures with frictional interfaces, in: M.R. Brake (Ed.), The Mechanics of Jointed Structures: Recent Research and Open Challenges for Developing Predictive Models for Structural Dynamics, Springer International Publishing, Cham, 2018, pp. 427–450, http://dx.doi.org/10.1007/978-3-319-56818-8_24.

[9] J. Yuan, F. El-Haddad, L. Salles, C. Wong, Numerical assessment of reduced order modeling techniques for dynamic analysis of jointed structures with contact nonlinearities, Trans. ASME, J. Eng. Gas Turbines Power 141 (3) (2019) 031027, http://dx.doi.org/10.1115/1.4041147.

[10] E. Petrov, Method for direct parametric analysis of nonlinear forced response of bladed disks with friction contact interfaces, Trans. ASME, J. Turbomach. 126 (4) (2004) 654–662, http://dx.doi.org/10.1115/1.1776588.

[11] E. Petrov, Sensitivity analysis of nonlinear forced response for bladed discs with friction contact interfaces, in: Turbo Expo: Power for Land, Sea, and Air, Vol. 47276, 2005, pp. 483–494, http://dx.doi.org/10.1115/GT2005-68935.

[12] M. Krack, S. Tatzko, L. Panning-von Scheidt, J. Wallaschek, Reliability optimization of friction-damped systems using nonlinear modes, J. Sound Vib. 333 (13) (2014) 2699–2712, http://dx.doi.org/10.1016/j.jsv.2014.02.008.

[13] M. Brake, Contact modeling across scales: from materials to structural dynamics applications, J. Struct. Dyn. (2021) URL https://popups.uliege.be/2684-6500/index.php?id=72.

[14] W. Tang, B.I. Epureanu, Geometric optimization of dry friction ring dampers, Int. J. Non-Linear Mech. 109 (2019) 40–49, http://dx.doi.org/10.1016/j.ijnonlinmec.2018.11.001.

[15] L. Panning, W. Sextro, K. Popp, Optimization of the contact geometry between turbine blades and underplatform dampers with respect to friction damping, in: Turbo Expo: Power for Land, Sea, and Air, Vol. 36096, 2002, pp. 991–1002, http://dx.doi.org/10.1115/GT2002-30429.

[16] M. Hüls, L. Panning-von Scheidt, J. Wallaschek, Influence of geometric design parameters onto vibratory response and high-cycle fatigue safety for turbine blades with friction damper, Trans. ASME, J. Eng. Gas Turbines Power 141 (4) (2019) http://dx.doi.org/10.1115/1.4040732.

[17] Y. Yuan, A. Jones, R. Setchfield, C. Schwingshackl, Robust design optimisation of underplatform dampers for turbine applications using a surrogate model, J. Sound Vib. 494 (2021) 115528, http://dx.doi.org/10.1016/j.jsv.2020.115528.

[18] J.A. Greenwood, J.P. Williamson, Contact of nominally flat surfaces, Proc. R. Soc. Lond. Ser. A Math. Phys. Eng. Sci. 295 (1442) (1966) 300–319, http://dx.doi.org/10.1098/rspa.1966.0242.

[19] S. Medina, D. Nowell, D. Dini, Analytical and numerical models for tangential stiffness of rough elastic contacts, Tribol. Lett. 49 (1) (2013) 103–115, http://dx.doi.org/10.1007/s11249-012-0049-y.

[20] M. Eriten, A. Polycarpou, L. Bergman, Physics-based modeling for partial slip behavior of spherical contacts, Int. J. Solids Struct. 47 (18–19) (2010) 2554–2567, http://dx.doi.org/10.1016/j.ijsolstr.2010.05.017.

[21] D. Zhang, Y. Xia, F. Scarpa, J. Hong, Y. Ma, Interfacial contact stiffness of fractal rough surfaces, Sci. Rep. 7 (1) (2017) 1–9, http://dx.doi.org/10.1038/s41598-017-13314-2.

[22] N.N. Balaji, W. Chen, M.R. Brake, Traction-based multi-scale nonlinear dynamic modeling of bolted joints: Formulation, application, and trends in micro-scale interface evolution, Mech. Syst. Signal Process. 139 (2020) 106615, http://dx.doi.org/10.1016/j.ymssp.2020.106615.

[23] J. Armand, L. Salles, C. Schwingshackl, D. Süß, K. Willner, On the effects of roughness on the nonlinear dynamics of a bolted joint: a multiscale analysis, Eur. J. Mech. A Solids 70 (2018) 44–57, http://dx.doi.org/10.1016/j.euromechsol.2018.01.005.

[24] M. Allara, S. Zucca, M.M. Gola, Effect of crowning of dovetail joints on turbine blade root damping, in: Key Engineering Materials, Vol. 347, Trans Tech Publ, 2007, pp. 317–322, http://dx.doi.org/10.4028/www.scientific.net/KEM.347.317.

[25] L. Pesaresi, L. Salles, A. Jones, J. Green, C. Schwingshackl, Modelling the nonlinear behaviour of an underplatform damper test rig for turbine applications, Mech. Syst. Signal Process. 85 (2017) 662–679, http://dx.doi.org/10.1016/j.ymssp.2016.09.007.

[26] C. Gastaldi, T.M. Berruti, M.M. Gola, The effect of surface finish on the proper functioning of underplatform dampers, J. Vib. Acoust. 142 (5) (2020) 051103, http://dx.doi.org/10.1115/1.4046954.

[27] L. Gallego, B. Fulleringer, S. Deyber, D. Nelias, Multiscale computation of fretting wear at the blade/disk interface, Tribol. Int. 43 (4) (2010) 708–718, http://dx.doi.org/10.1016/j.triboint.2009.10.011.

[28] L.A.c. Salles, L. Blanc, F. Thouverez, A.M. Gouskov, P. Jean, Dynamic analysis of a bladed disk with friction and fretting-wear in blade attachments, in: ASME Turbo Expo 2009: Power for Land, Sea, and Air, American Society of Mechanical Engineers, 2009, pp. 465–476, http://dx.doi.org/10.1115/GT2009-60151.

[29] L. Salles, L. Blanc, F. Thouverez, A.M. Gouskov, Dynamic analysis of fretting-wear in friction contact interfaces, Int. J. Solids Struct. 48 (10) (2011) 1513–1524, http://dx.doi.org/10.1016/j.ijsolstr.2011.01.035.

[30] J. Armand, L. Pesaresi, L. Salles, C. Wong, C.W. Schwingshackl, A modelling approach for the nonlinear dynamics of assembled structures undergoing fretting wear, Proc. R. Soc. Lond. Ser. A Math. Phys. Eng. Sci. 475 (2223) (2019) 20180731, http://dx.doi.org/10.1098/rspa.2018.0731.

[31] R.M. Rosenberg, Normal modes of nonlinear dual-mode systems, J. Appl. Mech. 27 (2) (1960) 263–268, http://dx.doi.org/10.1115/1.3643948.

[32] S.W. Shaw, C. Pierre, Non-linear normal modes and invariant manifolds, J. Sound Vib. 150 (1) (1991) 170–173, http://dx.doi.org/10.1016/0022-460X(91)90412-D.

[33] M. Krack, Nonlinear modal analysis of nonconservative systems: Extension of the periodic motion concept, Comput. Struct. 154 (2015) 59–71, http://dx.doi.org/10.1016/j.compstruc.2015.03.008.

[34] D. Laxalde, F. Thouverez, Complex non-linear modal analysis for mechanical systems: Application to turbomachinery bladings with friction interfaces, J. Sound Vib. 322 (4–5) (2009) 1009–1025, http://dx.doi.org/10.1016/j.jsv.2008.11.044.

[35] Y. Sun, J. Yuan, A. Vizzaccaro, L. Salles, Comparison of different methodologies for the computation of damped nonlinear normal modes and resonance prediction of systems with non-conservative nonlinearities, Nonlinear Dynam. (2021) 1–31, http://dx.doi.org/10.1007/s11071-021-06567-0.

[36] M. Jahn, S. Tatzko, L. Panning-von Scheidt, J. Wallaschek, Comparison of different harmonic balance based methodologies for computation of nonlinear modes of non-conservative mechanical systems, Mech. Syst. Signal Process. 127 (2019) 159–171, http://dx.doi.org/10.1016/j.ymssp.2019.03.005.

[37] M. Krack, Extension of the single-nonlinear-mode theory by linear attachments and application to exciter-structure interaction, J. Sound Vib. 505 (2021) 116120, http://dx.doi.org/10.1016/j.jsv.2021.116120.

[38] Y. Sun, A. Vizzaccaro, J. Yuan, L. Salles, An extended energy balance method for resonance prediction in forced response of systems with non-conservative nonlinearities using damped nonlinear normal mode, Nonlinear Dynam. 103 (4) (2021) 3315–3333, http://dx.doi.org/10.1007/s11071-020-05793-2.

[39] J. Yuan, Y. Sun, C. Schwingshackl, L. Salles, Computation of damped nonlinear normal modes for large scale nonlinear systems in a self-adaptive modal subspace, Mech. Syst. Signal Process. 162 (2022) 108082, http://dx.doi.org/10.1016/j.ymssp.2021.108082.

[40] H. Festjens, G. Chevallier, J.-l. Dion, A numerical tool for the design of assembled structures under dynamic loads, Int. J. Mech. Sci. 75 (2013) 170–177, http://dx.doi.org/10.1016/j.ijmecsci.2013.06.013.
[41] R.M. Lacayo, M.S. Allen, Updating structural models containing nonlinear Iwan joints using quasi-static modal analysis, Mech. Syst. Signal Process. 118 (2019) 133–157, http://dx.doi.org/10.1016/j.ymssp.2018.08.034.
[42] N.N. Balaji, M.R. Brake, A quasi-static non-linear modal analysis procedure extending Rayleigh quotient stationarity for non-conservative dynamical systems, Comput. Struct. 230 (2020) 106184, http://dx.doi.org/10.1016/j.compstruc.2019.106184.
[43] J. Yuan, L. Salles, F. El Haddad, C. Wong, An adaptive component mode synthesis method for dynamic analysis of jointed structure with contact friction interfaces, Comput. Struct. 229 (2020) 106177, http://dx.doi.org/10.1016/j.compstruc.2019.106177.
[44] J. Yuan, C. Schwingshackl, C. Wong, L. Salles, On an improved adaptive reduced-order model for the computation of steady-state vibrations in large-scale non-conservative systems with friction joints, Nonlinear Dynam. 103 (4) (2021) 3283–3300, http://dx.doi.org/10.1007/s11071-020-05890-2.
[45] J. Yuan, L. Salles, C. Schwingshackl, Effects of the geometry of friction interfaces on the nonlinear dynamics of jointed structure, in: Nonlinear Structures & Systems, Volume 1, Springer, 2022, pp. 67–74, http://dx.doi.org/10.1007/978-3-030-77135-5_7.
[46] C. Schwingshackl, F. Zolfi, D. Ewins, A. Coro, R. Alonso, Nonlinear friction damping measurements over a wide range of amplitudes, in: Proceedings of the International Modal Analysis Conference XXVII, Orlando, 2009.
[47] J. Armand, L. Pesaresi, L. Salles, C. Schwingshackl, A multiscale approach for nonlinear dynamic response predictions with fretting wear, Trans. ASME, J. Eng. Gas Turbines Power 139 (2) (2017) 022505, http://dx.doi.org/10.1115/1.4034344.
[48] J. Armand, L. Salles, C. Schwingshackl, Numerical simulation of partial slip contact using a semi-analytical method, in: ASME 2015 International Design Engineering Technical Conferences and Computers and Information in Engineering Conference, American Society of Mechanical Engineers, 2015, http://dx.doi.org/10.1115/DETC2015-46464, V008T13A022.
[49] I.A. Polonsky, L.M. Keer, Fast methods for solving rough contact problems: A comparative study, J. Tribol. 122 (1) (2000) 36, http://dx.doi.org/10.1115/1.555326.
[50] K.L. Johnson, Contact Mechanics, Cambridge University Press, 1985, Cambridge Books Online.
[51] A.E.H. Love, A Treatise on the Mathematical Theory of Elasticity, University Press, 1906.
[52] J. Armand, Nonlinear Dynamics of Jointed Structures: A Multiscale Approach to Predict Fretting Wear and its Effects on the Dynamic Response, Imperial College London, 2017.
[53] A. Fantetti, Tamatam, Volvert, Laval, Liu, L. Salles, M. Brake, C. Schwingshackl, D. Nowell, The impact of fretting wear on structural dynamics: experiment and simulation, Tribol. Int. 138 (2019) 111–124, http://dx.doi.org/10.1016/j.triboint.2019.05.023.
[54] J. Yuan, A. Fantetti, E. Denimal, S. Bhatnagar, L. Pesaresi, C. Schwingshackl, L. Salles, Propagation of friction parameter uncertainties in the nonlinear dynamic response of turbine blades with underplatform dampers, Mech. Syst. Signal Process. 156 (2021) 107673, http://dx.doi.org/10.1016/j.ymssp.2021.107673.
[55] J. Yuan, L. Salles, C. Wong, S. Patsias, A novel penalty-based reduced order modelling method for dynamic analysis of joint structures, in: IUTAM Symposium on Model Order Reduction of Coupled Systems, Stuttgart, Germany, May 22–25, 2018, http://dx.doi.org/10.1007/978-3-030-21013-7_12.
[56] E. Sarrouy, J.-J. Sinou, Non-linear periodic and quasi-periodic vibrations in mechanical systems-on the use of the harmonic balance methods, in: Advances in Vibration Analysis Research, InTech, 2011, http://dx.doi.org/10.5772/15638.
[57] G. Sinclair, N. Cormier, J. Griffin, G. Meda, Contact stresses in dovetail attachments: finite element modeling, Trans. ASME, J. Eng. Gas Turbines Power 124 (1) (2002) 182–189, http://dx.doi.org/10.1115/1.1391429.
[58] G. Sinclair, N. Cormier, Contact stresses in dovetail attachments: alleviation via precision crowning, Trans. ASME, J. Eng. Gas Turbines Power 125 (4) (2003) 1033–1041, http://dx.doi.org/10.1115/1.1584477.
[59] S. Fouvry, C. Paulin, An effective friction energy density approach to predict solid lubricant friction endurance: Application to fretting wear, Wear 319 (1–2) (2014) 211–226, http://dx.doi.org/10.1016/j.wear.2014.07.009.
[60] K. Barman, P. Shipway, K. Voisey, G. Pattinson, The role of a thermally sprayed cuniin underlayer in the durability of a dry-film lubricant system in fretting–a phenomenological model, Tribol. Int. 123 (2018) 307–315, http://dx.doi.org/10.1016/j.triboint.2018.03.018.
[61] Y.-P. Zhu, J. Yuan, Z.-Q. Lang, C.W. Schwingshackl, L. Salles, V. Kadirkamanathan, The data-driven surrogate model-based dynamic design of aeroengine fan systems, Trans. ASME, J. Eng. Gas Turbines Power 143 (10) (2021) http://dx.doi.org/10.1115/1.4049504.